

Speed limits for radiation driven SMBH winds

A. Luminari^{1,2}, F. Nicastro^{2,3}, M. Elvis³, E. Piconcelli², F. Tombesi^{1,2,4,5}, L. Zappacosta², F. Fiore⁶,

¹ Department of Physics, University of Rome “Tor Vergata”, Via della Ricerca Scientifica 1, I-00133 Rome, Italy
e-mail: alfredo.luminari@inaf.it

² INAF - Osservatorio Astronomico di Roma, Via Frascati 33, I-00078 Monte Porzio Catone, Italy

³ Harvard-Smithsonian Center for Astrophysics, 60 Garden Street, Cambridge, MA 02138, USA

⁴ Department of Astronomy, University of Maryland, College Park, MD 20742, USA

⁵ NASA - Goddard Space Flight Center, Code 662, Greenbelt, MD 20771, USA

⁶ INAF - Osservatorio Astronomico di Trieste, Via G. B. Tiepolo 11, I-34143 Trieste, Italy

Received xxyyzz; accepted xxyyzz

ABSTRACT

Context. Ultra Fast Outflows (UFOs) have become an established feature in X-ray spectra of Active Galactic Nuclei (AGN). According to the standard picture, they are launched at accretion disc scales with relativistic velocities, up to 0.3-0.4 times the speed of light. Their high kinetic power is enough to induce an efficient feedback on galactic-scale, possibly contributing to the co-evolution between the central supermassive black hole (SMBH) and the host galaxy. It is therefore of paramount importance to fully understand the UFO physics, and in particular the forces driving their acceleration and the relation with the accretion flow from which they originate.

Aims. In this paper, we investigate the impact of special relativity effects on the radiative pressure exerted onto the outflow. The radiation received by the wind decreases for increasing outflow velocity v , implying that the standard Eddington limit argument has to be corrected according to v . Due to the limited ability of the radiation to counteract the black hole gravitational attraction, we expect to find lower typical velocities with respect to the non-relativistic scenario.

Methods. We integrate the relativistic-corrected outflow equation of motion for a realistic set of starting conditions. We concentrate on a range of ionisations, column densities and launching radii consistent with those typically estimated for UFOs. We explore a one-dimensional, spherical geometry and a three-dimensional setting with a rotating thin accretion disc.

Results. We find that the inclusion of special relativity effects leads to sizeable differences in the wind dynamics and that v is reduced up to 50 % with respect to the non-relativistic treatment. We compare our results with a sample of UFO from the literature, and we find that the relativistic-corrected velocities are systematically lower than the reported ones, indicating the need for an additional mechanism, such as magnetic driving, to explain the highest velocity components. We note that these conclusions, derived for AGN winds, have a general applicability.

Key words. accretion, accretion disks - black hole physics - quasars: supermassive black holes - quasars: absorption lines - opacity - relativistic processes

1. Introduction

Fast outflows, and in particular Ultra Fast Outflows (UFOs), are routinely observed in Active Galactic Nuclei (AGN) as blueshifted absorption and emission features imprinted on the X-ray spectrum, with velocities ranging from ~ 0.03 to $0.4 - 0.5$ times the speed of light c (Tombesi et al. 2011, 2015; Nardini et al. 2015; Fiore et al. 2017; Parker et al. 2017). They are launched at accretion disc scales from the central supermassive black hole (SMBH) and may display a kinetic power as high as 20-40 % of the bolometric luminosity of the AGN (Feruglio et al. 2015; Nardini et al. 2015; Nardini & Zubovas 2018; Laurenti et al. 2020), which is more than enough to trigger a massive feedback in the host galaxy, according to theoretical models (Di Matteo et al. 2005; Hopkins & Elvis 2010; Gaspari et al. 2011).

Despite their crucial importance in the framework of the co-evolution between the host galaxy and the SMBH (Kormendy & Ho 2013), the physics of these outflows, and particularly their acceleration mechanism, still remains mostly unknown. According to one of the most accepted scenarios, the gas is accelerated through the pressure of the radiation emitted in the vicinity of the central black hole, even though it is not yet fully clear up to which velocities this mechanism can be effective (Proga & Kall-

man 2004; Higginbottom et al. 2014; Hagino et al. 2015; King & Pounds 2015).

Similarly, broad absorption lines (BALs) in the UV regime are observed in $\sim 10 - 20\%$ of optically selected quasars. Their velocities can be up to $0.3c$ and are located at parsec-scales from the SMBH (Hamann et al. 2018; Bruni et al. 2019), thus representing another potential energy input for a galactic-scale feedback. As for the X-ray winds, radiative driving has been suggested as their main driver (Elvis 2000; Matthews et al. 2020)

In a recent paper, Luminari et al. (2020) discussed the importance of special relativity effects when the wind outflow velocity becomes mildly relativistic, $v \gtrsim 0.05c$. In fact, due to the space-time transformation, the amount of radiative power received by the fast wind decreases with increasing v : with respect to a layer of gas at rest, the amount of radiation impinging on the wind is reduced of $\sim 30\%$ for $v = 0.1c$, and of $\sim 90\%$ for $v = 0.5c$. This implies that the classical derivation of the radiative pressure for a static gas is no longer valid for high velocity winds; accordingly, the radiative driving scenario has to be revised to incorporate these effects.

In this Paper we integrate the equation of motion for a wind launched at accretion disc scales in order to assess the impact

of special relativity effects on radiative acceleration. We will mainly focus on X-ray winds; however, our results applies also for BAL winds. In Sect. 2 we present a simple, one-dimensional model of a wind illuminated by a luminosity corresponding to the Eddington value and we demonstrate that, owing to these effects, radiation alone is not able to counteract the gravitational attraction of the SMBH. In Sect. 3 we present a three-dimensional scenario in which the gas is lifted from a geometrically thin accretion disk and it is radiatively accelerated. We refine this model in Sect. 4 and Sect. 5 with a more detailed treatment of the wind opacity. We present the results in Sect. 6 and we discuss them in Sect. 7. Finally, we summarise our results in Sect. 8.

2. One-dimensional, spherically symmetric wind model

In order to have a glimpse on the importance of special relativity effects, we start from a simple toy model as follows. We assume that all the luminosity comes from a central point source and the gas has an initial velocity v_0 at a distance r_0 from the centre. We solve the equation of motion along the radial coordinate r . According to the Euler momentum equation, the force exerted by a radiative pressure gradient ∇p on an infinitesimal wind element with density ρ is:

$$\rho \frac{dv}{dt} = \nabla p - \frac{GM\rho}{r^2} \quad (1)$$

where $\frac{dv}{dt}$ is the wind acceleration and G, M are the gravitational constant and the SMBH mass, respectively. For the sake of simplicity, we assume for the moment that i) the wind is optically thin and ii) its opacity is dominated by the Thomson cross-section. We will relax these assumptions in the following. This way, we obtain an equation of motion for the wind:

$$\frac{dv}{dt} = \frac{L'k}{4\pi r^2 c} - \frac{GM}{r^2} \quad (2)$$

Where L' is the central luminosity in the wind reference frame K' and k is the opacity of the wind, that we approximate as $k = \frac{\sigma_T}{m_p}$, where σ_T, m_p are the Thomson cross-section and the proton mass, respectively (Rybicki & Lightman 1986). In the definition of L' we include special relativity effects as described in Luminari et al. (2020), so that $L' = L \cdot \Psi$, where L is the luminosity in the source frame K and $\Psi \equiv \psi^4 = \frac{1}{\gamma^4(1+\beta\cos(\theta))^4}$, where γ is the Lorentz factor, $\beta = \frac{v}{c}$ and θ is the angle between the velocity of the gas and the incident luminosity L .

For a wind that is moving radially outward, $\theta = 0deg$, the luminosity can be written as $L' = L \frac{(1-\beta)^2}{(1+\beta)^2}$. We can rewrite Eq. 2 as:

$$\frac{dv}{dt} = L \frac{(1-\beta)^2}{(1+\beta)^2} \frac{\sigma_T}{4\pi r^2 c m_p} - \frac{GM}{r^2} \quad (3)$$

Where r and β are functions of v itself. The complete set of equations, including initial conditions, can be written as:

$$\frac{dv}{dt} = L \frac{(1 - \frac{v}{c})^2}{(1 + \frac{v}{c})^2} \frac{\sigma_T}{4\pi r(t)^2 c m_p} - \frac{GM}{r^2} \quad (4a)$$

$$r(t) = r_0 + \int_{t_0}^{t_1} v dt \quad (4b)$$

$$r_0 = r(t = t_0) \quad (4c)$$

$$v_0 = v(t = t_0) \quad (4d)$$

Where t_0, t_1 are the starting and ending time of the numerical integration, respectively. Moreover, we assume that the launching velocity of the wind v_0 corresponds to the rotational velocity of an accretion disc, orbiting around the black hole with a Keplerian profile, at $r = r_0$, so that $v_0 = \sqrt{\frac{GM}{r_0}}$. Albeit this choice of v_0 may seem arbitrary at this point, it will be useful to compare the results with those of the following Sections. We also note that the escape velocity at $r = r_0$ is equal to $\sqrt{\frac{2GM}{r_0}} = \sqrt{2}v_0$. We can rewrite Eqs. 4 as:

$$\frac{dv}{dt} = \left(\lambda_{Edd} \frac{(1-v)^2}{(1+v)^2} - 1 \right) \frac{1}{r(t)^2} \quad (5a)$$

$$r(t) = r_0 + \int_{t_0}^{t_1} v dt \quad (5b)$$

$$r_0 = r(t = t_0) \quad (5c)$$

$$v_0 = \sqrt{\frac{1}{r_0}} \quad (5d)$$

where $\lambda_{Edd} \equiv L/L_{Edd}$ is the luminosity in units of the Eddington luminosity $L_{Edd} = \frac{4\pi GMm_p c}{\sigma_T}$, r, t are in units of the gravitational radius and time, $r_G = \frac{GM}{c^2}$, $t_G = \frac{r_G}{c}$ respectively, and v is in units of c . We span the interval between 5 and 500 r_G for r_0 , to encompass the typical launching radius of UFOs, which usually lies between ~ 50 and some hundreds r_G (Tombesi et al. 2012, 2013; Nardini et al. 2015; Tombesi et al. 2015; Laurenti et al. 2020). We divide this interval in five logarithmically-spaced steps: $r_0 \in [5.0, 15.8, 50.0, 158.1, 500.0]r_G$. As we will discuss in detail in Sect. 5, we note that the assumption of a point source may be less accurate for launching radii smaller than $50.0r_G$. Nonetheless, it is instructive to study the solutions down to the smallest radii to identify possible trends. We integrate the equation for $10^6 t_G$, after which the dynamics of the wind reaches a steady state and the velocity appears to be almost constant in all the cases. We note that $10^6 t_G$ corresponds to $\sim 1(100)yr_s$ for $M = 10^7(10^9)M_{sun}$, while present-day X-ray observations have observation times smaller than a month. This will allow us to follow the wind dynamics for a sufficient time scale to compare with the observations for any value of M inside the typical AGN range. We find that the wind evolution is best sampled by a logarithmic time grid, rather than by linear steps. We fix the number of time elements to $5 \cdot 10^6$ to obtain an optimal numerical accuracy. Using a higher resolution does not produce noticeable improvements in the solutions.

We show in Figure 1 the numerical result of Eqs. 5 for $\lambda_{Edd} = 1$. For comparison, we also show the classic analogue of Eq. 5, i.e., without the luminosity reduction factor Ψ due to relativistic effects. Hereafter, we will indicate with solid(dashed) lines the values relative to the relativistic(classic) treatment, if not stated otherwise. Since we input a luminosity corresponding to the Eddington limit, $\lambda_{Edd} = 1$, in the classic case the radiative pressure is able to counteract (by definition) the gravitational pull from the black hole. As a result, the acceleration of the gas is null and we obtain constant velocity solutions. Once the wind is launched with a given v_0 , it escapes from the system with constant $v = v_0$, as can be seen in the right panel of Fig. 1.

As expected, relativistic effects reduce radiation pressure, resulting in a deceleration of the wind under the gravitational pull of the SMBH. Indeed, it can be seen that the wind trajectories, especially the ones at smaller radii (i.e., closer to the black hole) undergo a significant velocity reduction. In the extreme case of $r_0 = 5r_G$, the velocity drops to 0. When $v = 0$, relativistic ef-

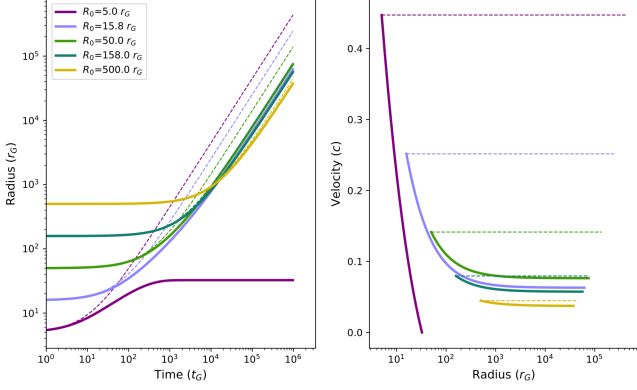


Fig. 1: Left: radial distance from the black hole $r(t)$ as a function of t for $\lambda_{Edd} = 1$ and $v_0 = v_{rot} = \sqrt{\frac{GM}{r_0}}$; Right: radial velocity $v(t)$ as a function of $r(t)$. Solid lines indicate the trajectories in the relativistic framework (Eqs. 5), while dashed lines correspond to the classic (i.e., non-relativistic) ones.

fects vanish and radiation pressure is able, as in the classic case, to sustain the wind against the gravitational force, leading to a "stalling wind". The highest final velocity is given by the case with $r_0 = 50.0r_G$ and it is $\approx 0.1c$, consistent with the typical observed UFO velocities (e.g., Tombesi et al. 2011; Gofford et al. 2015).

3. Axisymmetric wind launched from an accretion disk

Let us now rewrite Eq. 5 in the case of a wind launched from an accretion disc. We assume axisymmetry and a geometrically thin disc, such as in Shakura & Sunyaev (1973), orbiting with a Keplerian profile. We adopt a cylindrical coordinate system (R, ϕ, z) . The set of equations is then:

$$\frac{dv_R}{dt} = \left(\frac{\lambda_{Edd}}{\gamma^4(1 + \beta \cos\theta)^4} - 1 \right) \frac{R}{r^3} + \frac{l^2}{R^3} \quad (6a)$$

$$\frac{dv_z}{dt} = \left(\frac{\lambda_{Edd}}{\gamma^4(1 + \beta \cos\theta)^4} - 1 \right) \frac{z}{r^3} \quad (6b)$$

$$R = R_0 + \int_{t_0}^{t_1} v_R dt \quad (6c)$$

$$z = \int_{t_0}^{t_1} v_z dt \quad (6d)$$

$$r = \sqrt{R^2 + z^2} \quad (6e)$$

$$\mathbf{v}_0 = \mathbf{v}(t = t_0) = (0, v_{rot}, v_{z,0}) \quad (6f)$$

$$\mathbf{r}_0 = \mathbf{r}(t = t_0) = (R_0, 0, 0) \quad (6g)$$

where, as in Eqs. 5, r, t are in units of r_G, t_G , θ is the angle between the incident luminosity and the direction of motion of the gas and we assume that the luminosity source is point-like. Hereafter, we indicate in bold the vectorial quantities. In the first two equations, the second term in the right-hand bracket corresponds to the gravitational attraction. l is the specific angular momentum (angular momentum per unit mass), which is a conserved quantity during the motion. $\mathbf{r}_0, \mathbf{v}_0$ are the starting radius and velocity, respectively. We assume that, initially, the gas lies on the disk plane and the starting velocity lifts the gas above the disk, along

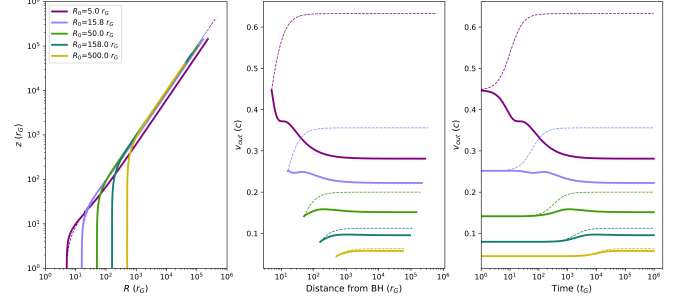


Fig. 2: Wind trajectories for $v_{z,0} = v_{rot}$ and $\lambda_{Edd} = 1$ in axisymmetric geometry. From left to right: trajectories of the wind in the $z-R$ plane (x-axis corresponds to the radius and y-axis to the altitude from the disc plane); outflow velocity v_{out} as a function of r (where $r = \sqrt{R^2 + z^2}$, $v_{out} = \sqrt{v_R^2 + v_z^2}$); v_{out} as a function of t . Solid (dashed) lines refer to the relativistic(classic) treatment.

the z coordinate, with a velocity proportional to the disc rotational velocity $v_{rot} = \sqrt{\frac{l}{R_0}}$. The velocity along the ϕ coordinate is updated at each step to ensure the conservation of l . These initial conditions are rather general, and represents a good approximation of the radiatively-driven wind scenario (Proga & Kallman 2000; Proga & Kallman 2004), as well as the magneto-hydrodynamic (MHD) scenario, in which the gas is lifted through magnetic field lines co-rotating with the disk (Blandford & Payne 1982; Contopoulos & Lovelace 1994; Fukumura et al. 2010, 2014; Cui & Yuan 2020).

Fig. 2 shows the solutions of Eqs. 6 for $R_0 = [5.0, 15.8, 50.0, 158.1, 500.0]r_G$, an integration time of $10^6 t_G$, a logarithmic temporal resolution of $5 \cdot 10^6$ steps, as in Sect. 2, $\lambda_{Edd} = 1$ and $v_{z,0} = v_{rot}$. For comparison, we also show the corresponding classic solutions. As expected, the highest differences are observed at smaller radii, where the velocity is higher and the relativistic effects are stronger. We present in Fig. A.1 in the Appendix a detailed plot of the wind dynamics.

Hereafter, we concentrate on the outflow velocity, defined as $v_{out} = \sqrt{v_R^2 + v_z^2}$, rather than on the total wind velocity $v = \sqrt{v_R^2 + v_\phi^2 + v_z^2}$, to better compare our results with observations. The velocity of the observed UFOs is primarily derived through spectroscopy, thanks to the Doppler shift of the wind absorption lines. These lines are usually described with Gaussian or Voigt profiles, i.e. they have an average energy and some degree of broadening. The observed wind outflow velocity v_{obs} is usually derived from the average velocity, while the broadening is phenomenologically ascribed to turbulence or rotational motion within the wind.

In our model, v_{obs} is given by the projection of $\mathbf{v}_R + \mathbf{v}_z$ along the line of sight (LOS), while the rotational velocity v_ϕ only contributes to the broadening of the line, thanks to the axisymmetry of the system. The highest v_{obs} is given by v_{out} , and corresponds to the case in which the LOS is parallel to $\mathbf{v}_R + \mathbf{v}_z$. We refer to Fukumura & Tombesi (2019) for a detailed discussion on this point. Interestingly, the authors discuss the possibility that a rotational motion of the wind around the X-ray corona is responsible for the broadening of the absorption lines, in a similar fashion to the discussion here.

4. Force multipliers

In the accretion disc wind literature, the wind opacity is usually calculated analytically over a broad range of absorption lines in the UV and X-ray energy range (see e.g. Proga & Kallman 2004; Risaliti & Elvis 2010; Sim et al. 2010; Dyda & Proga 2018; Quera-Bofarull et al. 2020), obtaining the so-called "force multipliers". Here, we use the radiative transfer code *XSTAR* (Kallman & Bautista 2001). Saez & Chartas (2011); Chartas et al. (2009) performed calculations in a similar fashion using *Cloudy* photoionisation code (Ferland et al. 2017), albeit with a different formalism.

XSTAR accurately computes the transmitted spectrum S_T through a gas layer, as a function of the following input quantities:

- S_I , the incident spectrum, and its integrated ionising luminosity L_I^{ion} in the 1-1000 Ry interval (1 Ry = 13.6 eV).
- r_0 , the distance of the gas from the central luminosity source
- n_0 , the gas number density at r_0
- N_H , its column density
- α , the coefficient regulating the radial dependence of n : $n = n_0 \left(\frac{r_0}{r}\right)^\alpha$
- v_{broad} , the gas velocity dispersion regulating the broadening of the absorption features.

The difference $L_I - L_T$ (where L_I, L_T are the integrated luminosity of S_I, S_T) corresponds to the amount of radiation absorbed by the wind thanks to its opacity. This difference corresponds to a momentum Δp deposited on the wind, which can be written as $\Delta p = \frac{L_I - L_T}{c} = \frac{L_I \cdot f_{rad}}{c}$, where we introduce the new variable $f_{rad} = \frac{L_I - L_T}{L_I}$. Specifically, for a given set of initial parameters [$S_I, r_0, n_0, N_H, \alpha, v_{broad}$] we run an *XSTAR* simulation and we calculate f_{rad} as:

$$f_{rad} = \frac{\int_{E_0}^{E_1} s_v^I - s_v^T}{\int_{E_0}^{E_1} s_v^I} dv \quad (7)$$

where E_0, E_1 correspond to the lower and upper energy bound and s_v^I, s_v^T are the incident and transmitted flux, respectively, as functions of the frequency ν , so that $\int s_v^I dv = S_I$ and $\int s_v^T dv = S_T$. From a mathematical point of view, f_{rad} corresponds to a weighted average of the wind opacity. In all the cases of interest, absorption features are comprised in the energy interval between 0.1 eV and 100keV, that we choose as E_0, E_1 , respectively.

It is important to note that *XSTAR*, as well as other photoionisation codes such as *Cloudy*, does not allow the inclusion of a net velocity of the gas and the related relativistic effects. In order to take them into account, it is convenient to transform the spectra from the rest frame K to the wind reference frame K' , and to manipulate S_I and S_T , namely to shift their frequencies by a factor ψ and multiply their fluxes by ψ^3 (we refer to Luminari et al. 2020 for a detailed explanation). However, since f_{rad} is calculated as a ratio between S_T and S_I , the transformations cancel out so that f_{rad} can be directly calculated in K without the need of any relativistic transformation.

We integrate the equation of motion, Eq. 2, for a radial interval Δr , in which a wind column density N_H is enclosed, and we include the momentum Δp . The resulting equation is:

$$\begin{aligned} \frac{dv}{dt} &= \frac{\Delta p}{4\pi r^2 m_p N_H} + \frac{L'_{bol} \sigma_T}{4\pi r^2 c m_p} - \frac{GM}{r^2} \\ &= \frac{1}{4\pi r^2 c m_p} \cdot \left(\frac{L'_{UX} \cdot f_{rad}}{N_H} + L'_{bol} \cdot \sigma_T \right) - \frac{GM}{r^2} \end{aligned} \quad (8)$$

where we also include Thompson scattering and L'_{bol}, L'_{UX} correspond to the bolometric luminosity and the incident luminosity between E_0 and E_1 , respectively. The ' symbol indicates that the luminosities are in the K' frame, i. e. $L'_{bol}(L'_{UX}) = L_{bol}(L_{UX}) \cdot \frac{1}{\gamma^4(1+\beta \cos(\theta))^4}$. It must be noted that, for this equation to hold, Δr must be small enough so that r can be approximated as constant (i.e., $\Delta r \ll r$).

We put ourselves in the same framework of Sect. 3 (axisymmetry, thin accretion disk and conservation of l). The complete set of equations is then:

$$\frac{dv_R}{dt} = \left(\frac{\lambda'_{UX} \cdot f_{rad}}{\sigma_T N_H} + \lambda'_{Edd} - 1 \right) \frac{R}{r^3} + \frac{l^2}{(GM/c)^2 \cdot R^3} \quad (9a)$$

$$\frac{dv_z}{dt} = \left(\frac{\lambda'_{UX} \cdot f_{rad}}{\sigma_T N_H} + \lambda'_{Edd} - 1 \right) \frac{z}{r^3} \quad (9b)$$

$$R = R_0 + \int_{t_0}^{t_1} v_R dt \quad (9c)$$

$$z = \int_{t_0}^{t_1} v_z dt \quad (9d)$$

$$r = \sqrt{R^2 + z^2} \quad (9e)$$

$$v_0 = (0, v_{rot}, v_{z,0}) \quad (9f)$$

$$r_0 = (R_0, 0, 0) \quad (9g)$$

where, as in Sect. 3, r, t are in units of r_G, t_G and $\lambda'_{UX} \equiv L'_{UX}/L_{Edd}, \lambda'_{Edd} \equiv L'_{bol}/L_{Edd}$.

5. Initial parameters and force multipliers calculation

Since we are primarily interested in winds from AGN accretion discs, we focus on "typical" values of λ_{Edd} between 0.1 and 2.0 and a black hole mass $M = 10^8 M_{sun}$. However, as we show later in this section, the properties of the wind, and then the values of f_{rad} , mainly depend on λ_{Edd} , rather than on M or L_{bol} alone, so our results are applicable regardless of the black hole mass.

We use the bolometric corrections of Lusso et al. (2012) to obtain the 2-10 keV luminosities. We assume a simple powerlaw incident spectrum with photon index $\Gamma = 2$, consistent with the typical values observed in AGNs (Piconcelli et al. 2005; Tombesi et al. 2011), to extrapolate L_{ion} and L_{UX} .

Regarding the properties of the wind, we concentrate on a set of initial number density $\log(n_0/cm^3) \in [10, 11, 12, 13]$ in order to match the ionisation parameters of the observed UFOs, as we will discuss in the following, and a range of $N_H \in [5 \cdot 10^{22}, 10^{24}] cm^{-2}$. As starting radii we use the same set of values of Sect. 2 and 3: $R_0 \in [5.0, 15.8, 50.0, 158.1, 500.0] r_G$. In our picture, we assume that all the luminosity comes from a point source located at the coordinate origin ($R = 0, z = 0$). However, we note that observationally the X-ray flux is usually ascribed to a hot "corona", comprised within $\sim 10 r_G$ from the SMBH (Chartas et al. 2012; Reis & Miller 2013; Reis et al. 2014; Kara et al. 2016; Caballero-Garcia et al. 2020; Szanecki et al. 2020), while the UV radiation is due to the disc emissivity which, for a thin disc, has a peak at $\sim 20 r_G$ (Quera-Bofarull et al. 2020). As a result, we expect that in our code the radiative contribution may not be fully modelled for $R_0 < 50.0 r_G$; however, we include the cases for $R_0 = 5.0, 15.8 r_G$, since the fate of the wind is governed primarily by v_0 , rather than by the radiation pressure, as we will show later.

We fix α , the exponent regulating the radial dependence of n , to 2, so that $n = n_0 \left(\frac{r_0}{r}\right)^2$, as expected by mass conservation for

a medium expanding in a spherical geometry. Since we expect a high degree of velocity shear within the wind due to its acceleration, we use a high turbulent velocity $v_{broad} = 3000 \text{ km s}^{-1}$ to prevent line saturation. This value is consistent with those typically observed in UFOs (see e.g. Fukumura & Tombesi 2019 and references therein).

We briefly summarise here the range of input quantities of our simulations, from which we calculate a grid of f_{rad} values:

- λ_{Edd} : we divide the interval of interest in four values, logarithmically spaced: $\lambda_{Edd} = [0.1, 0.5, 1., 2.]$.
- n_0 : we divide the range in logarithmic steps: $\log(n_0/\text{cm}^3) \in [10, 11, 12, 13]$
- $r_0 \in [5.0, 15.8, 50.0, 158.1, 500.0]r_G$.
- N_H : we span the range $[5 \cdot 10^{22}, 10^{24}] \text{ cm}^{-2}$ with steps of $5 \cdot 10^{22} \text{ cm}^{-2}$.

We compute the geometrical thickness of the wind to check whether the $\Delta r \ll r$ condition in Eq. 4 is met. The results plotted in Fig. B.1 (first three panels) in Appendix show that $\Delta_R/R_0 < 1$ in all the cases. The only exception is for $R_0 = 5r_G, \log(n_0/\text{cm}^3) = 10$ when the column density is very high ($N_H > 7 \cdot 10^{23} \text{ cm}^{-2}$). However, as we will discuss later, the properties of the wind are quite independent from N_H , and we will focus on the typical UFO value of $N_H = 10^{23} \text{ cm}^{-2}$ (Tombesi et al. 2011) in most of the cases. In the last panel of Fig. B.1 we show the ionisation parameter $\xi(r)$, defined as $\frac{L_{ion}}{n_0 r_0^2}$, for $\lambda_{Edd} = 1.0, 0.1$.

This parameter is of great importance since the absorption structure of the wind, and then the values of f_{rad} , mainly depends on it. Our range of ξ , from $\sim 10^0$ to $\sim 10^6$, agrees well with the broad population of UFOs and Warm Absorbers (see e.g. Laha et al. 2014; Serafinelli et al. 2019); this, in turn, justifies our range of $\log(n_0)$. Moreover, our values for $\log(n_0)$ are in agreement with those commonly estimated for the Broad Line Region (BLR) and for UV and X-ray outflows (see e.g. Elvis 2000; Schurch & Done 2007; Saez & Chartas 2011; Netzer 2013). Finally, in Fig. B.2 we show the values of f_{rad} as a function of the wind parameters.

5.1. Impact of the initial parameters on the wind dynamics.

We solve the system of Eqs. 9 for the whole grid of initial parameters for an integration time of $10^6 t_G$, the same temporal resolution of Sect. 2 and using a set of $v_{z,0} \in [1.0, 10^{-1}, 10^{-2}, 10^{-3}] v_{rot}$. For a complete discussion of the results, we first analyse the impact of the different parameters. To characterise the wind dynamics, we define a wind successfully launched if it has a positive (outbound) velocity at the end of the integration time $t = t_1$, and we compute its terminal velocity as $v_t = v_{out}(t_1) = \sqrt{v_R(t_1)^2 + v_z(t_1)^2}$.

λ_{Edd} and $v_{z,0}$ are the dominant parameters, since they regulate the amount of radiation pressure and the initial velocity of the wind. When $v_{z,0} = v_{rot}$, the high initial velocity allows the wind to be successfully launched for any value of λ_{Edd} (albeit reaching different v_t). For $v_{z,0} = 10^{-1}, 10^{-2}, 10^{-3} v_{rot}$, instead, the impact of the initial velocity itself to the wind evolution is almost negligible, and the different solutions are indistinguishable between them. However, $v_{z,0}$ lifts the gas above the disk, displacing it from its equilibrium radius and exposing it to the radiation pressure. The fate of the wind will then depend on λ_{Edd} and, secondarily, on R_0 , but it is unaffected by the exact value of $v_{z,0}$. We plot in Fig. 3 the failed wind region (i.e., the radius up to which the wind cannot be successfully launched) as a function of λ_{Edd} , for different $v_{z,0}$. For $v_{z,0} = v_{rot}$, the wind is always

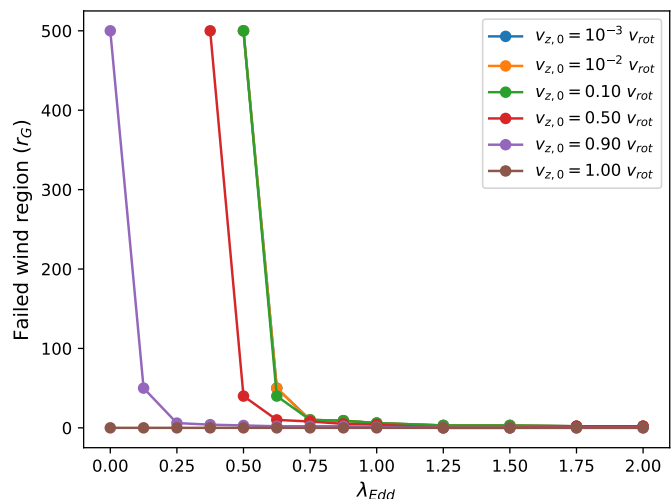


Fig. 3: Failed wind region as a function of λ_{Edd} for different $v_{z,0}$ (colour coding, see legend). It can be seen that for $v_{z,0} \leq 10^{-1} v_{rot}$ the region becomes quite constant, since the wind dynamics does not depend anymore on the value of $v_{z,0}$.

successful. Then, the failed region increases for decreasing $v_{z,0}$, and becomes quite constant for $v_{z,0} \leq 10^{-1} v_{rot}$. Please note that in this Figure we do not take into account wind opacity (i.e., we use the same treatment of Sect. 3) due to the long computational times required. However, the overall behaviour of $v_{z,0}$ is similar. For simplicity, from now on we will concentrate only on $v_{z,0} = [10^{-2}, 1.0] v_{rot}$. We note that $v_{z,0} = v_{rot}$ represents a remarkably high starting velocity, which could be justified only under certain particular physical conditions (see discussion in Sect. 7) and is significantly higher from the velocities commonly assumed in the literature, which are closer to the $v_{z,0} = 10^{-2} v_{rot}$ case (see e.g. Proga et al. 2000; Nomura et al. 2016, 2020). As we will detail in the following, we run the simulations using this starting value as a case study, in order to set an upper bound for the wind velocities that can be reached through radiative pressure, once corrected for relativistic effects.

For what concerns n_0 , it can give rise to differences in v_t of up to $0.05c$, but it generally does not affect the overall behaviour of the wind. Since f_{rad} is always roughly directly proportional to the column density, the wind solutions are also quite independent from N_H , because these two terms balance each other in the first term on the right-hand side of Eqs. 9a,b. We note that this trend holds also for optically-thick winds. In facts, for column densities $\approx \sigma_T^{-1} = 1.7 \cdot 10^{24} \text{ cm}^{-2}$, line opacity grows equally or less than linearly with N_H (Tombesi et al. 2011), and so the f_{rad}/N_H term in Eqs. 9a,b will not contribute more than for the optically-thin wind. We refer to Sect. C in the Appendix for further discussions on n_0, N_H . From now on we will focus on $\log(n_0/\text{cm}^3) = 11, N_H = 10^{23} \text{ cm}^{-2}$, if not stated otherwise.

6. Results

To examine the wind behaviour, we plot in Fig. 4 the trajectories in the $R - z$ plane for $\lambda_{Edd} = 0.1, 1.0$ (left and right panels, respectively). Hereafter, we convert the distance from the black hole (x -axis) from r_G to pc assuming $M = 10^8 M_{sun}$. As discussed in Sect. 5.1, the dominant parameter in the wind motion is $v_{z,0}$: for $v_{z,0} = v_{rot}$ (solid lines) the wind is always successful,

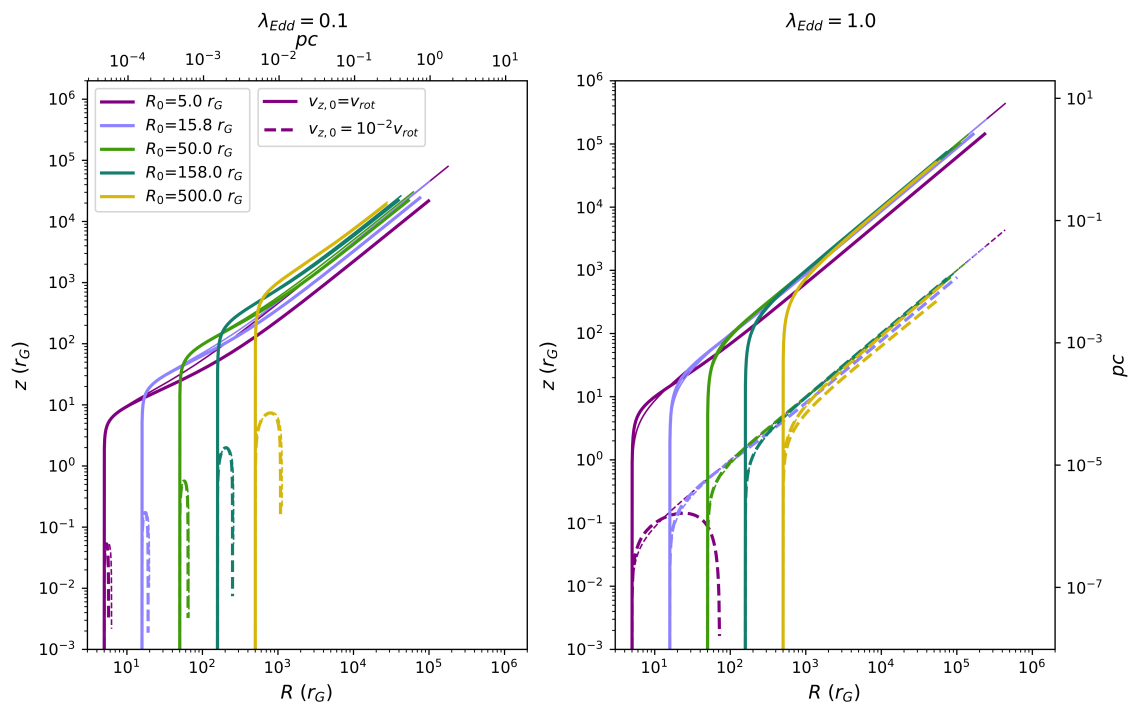


Fig. 4: Trajectories of the wind in the $z - R$ plane (y and x axis, respectively) for $\lambda_{Edd} = 0.1, 1.0$ (left and right panel, respectively). Solid(dashed) lines correspond to $v_{z,0} = v_{rot}(10^{-2}v_{rot})$. Thick and thin lines refer to the relativistic and classic (i.e., non-relativistic) treatment. Distances are reported both in units of r_G and pc , where the latter are calculated assuming $M = 10^8 M_{sun}$.

while when $v_{z,0} = 10^{-2}v_{rot}$ (dashed lines) it can be launched only for $\lambda_{Edd} = 1.0$ and $R_0 > 5r_G$. In Fig. 4 and in the followings, a truncated trajectory corresponds to a failed wind, since we interrupt the numerical integration when the gas falls back to the disk plane. Classic and relativistic trajectories (represented with bold and thin lines, respectively) are almost indistinguishable; however, as we will see in the following, their velocities are rather different.

In Fig. 5 we show a comparison between the velocities in the relativistic and in the classic treatments (bold and thin lines, respectively) as a function of t , for $\lambda_{Edd} = 0.1, 1.0$ (left and right panel, respectively). Purple, light blue and green lines corresponds to $R_0 = 5.0, 50.0, 500.0r_G$, respectively. Solid(dashed) lines correspond to $v_0 = 1.0(= 10^{-2}v_{rot})$. The impact of relativistic effects is remarkable, especially in the highest velocity cases. The maximum v_t drops from ≈ 0.6 to less than $0.3 c$ when taking into account the reduction of radiative pressure due to special relativity effects. We also note that, in most of the cases, the wind attains its terminal velocity within $10^4 t_G$ (corresponding to $0.1 yr$, i.e. roughly a month, for $M = 10^8 M_{sun}$). For $R_0 = 5r_G$, this time is reduced to $10^3 t_G$ ($10^{-2} yr$, i.e. a few days). For comparison, we indicate the times corresponding to one day and one month with vertical dotted lines.

In Fig. 6 we show the velocity of the wind as a function of the distance from the black hole. Line styles are as in Fig. 5. To give an idea of the dimensions of the accretion disc - torus system, we also indicate the typical distance at which BLR are observed and the dust sublimation radius, as a proxy of the inner boundary of the torus. We choose $0.01 pc$ as the BLR inner radius and $0.5 pc$ as the dust sublimation radius, which marks the boundary between the BLR and the torus (Coffey et al. 2014; Róžańska et al. 2014; Adhikari et al. 2016; Sturm et al. 2018; Czerny 2019).

For a detailed analysis of the wind dynamics, we show in Fig. D.1 in Appendix the case for $\lambda_{Edd} = 1, v_{z,0} = v_{rot}$.

7. Discussion

To have an idea of the overall behaviour of the wind, we plot (Fig. 7) v_t as a function of R_0 for $v_{z,0} = 10^{-2}, 1.0 v_{rot}$ (left and right panel). We also plot with dashed lines v_t obtained in the classic case. The null values indicate an unsuccessful wind. In order for the wind to attain the typical velocities of UFOs, i.e. $\geq 0.1c$ (see e.g. Fiore et al. 2017 for a collection of values from the literature), either the luminosity must be very high ($\lambda_{Edd} \geq 1.0$) or the initial velocity $v_{z,0}$, must be comparable to the rotational velocity v_{rot} .

In Fig. 8 we plot v_t as a function of ξ_0 (which is a monotonically decreasing function of R_0) in the densest and in the lightest cases, i.e. $\log(n_0/cm^3) = 10$ and $= 13$ for $\lambda_{Edd} = 0.1$ and $= 1.0$ (left and right panels, respectively). Generally, v_t is found to be a monotonically increasing function of ξ (see e.g. Tombesi et al. 2013). Interestingly, this behaviour can be reproduced only with $v_{z,0} \propto v_{rot}$.

We now compare our results with UFOs from the literature. Our goal is to establish whether the observed UFOs velocities can be reproduced within our radiative driving framework. To do so, we consider two different limiting velocities emerging from our results. The first one is the terminal velocity, v_t , which is almost reached by the wind after a very short time, and thus is the most likely to be observed. The second one is the maximum velocity reached by the wind, v_{max} , which is associated with the short-living, initial phases of the wind motion (see Figs. 5, 6), and hence represents an upper limit of the observable velocity. Since we are interested in the highest possible velocities, we focus on the $v_{z,0} = v_{rot}$ cases.

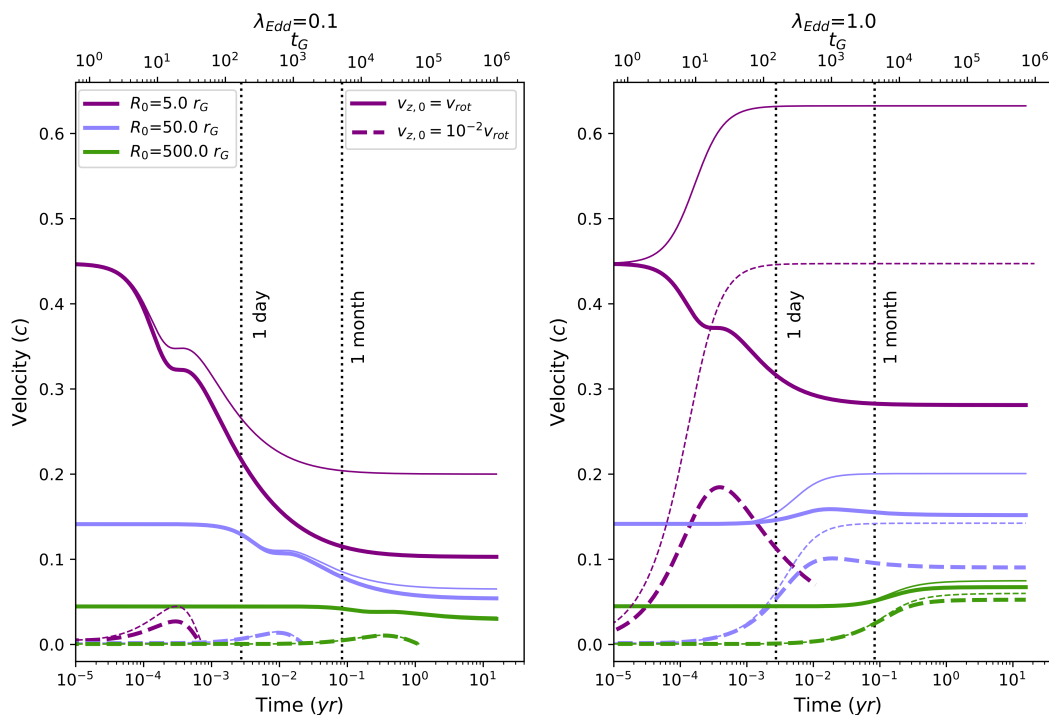


Fig. 5: Velocity of the wind as a function of t_G for $\lambda_{Edd} = 0.1, 1.0$ (left and right panel, respectively). Line styles as in Fig. 4. Times are converted from t_G to yr assuming $M = 10^8 M_{sun}$.

We compute the highest values of v_t, v_{max} as a function of λ_{Edd} for $R_0 \geq 50.0 r_G$, that represents a lower bound for the launching radius of the observed UFOs (see discussion in Sect. 2). We plot the results in Fig. 9, denoting with dark orange and blue the regions below the curves of v_t, v_{max} , respectively. These regions correspond to the allowed velocity ranges.

We show with different symbols (see legend) the location of several UFOs reported in the literature (see Sect. E in Appendix for references on the single sources). Interestingly, many points lie above the v_t (orange) allowed region, and many also above the v_{max} (blue) region. Such high velocities, which can be hardly explained within our radiative driving model, may lend support to other launching mechanisms. As discussed in Sect. 5.1, $v_{z,0} = v_{rot}$ represents an upper bound of the expected launching velocities for a radiatively-driven wind. Lower, physically-motivated $v_{z,0}$ would result in even lower limiting velocities than those reported in Fig. 9, thus strengthening our conclusion that radiative driving, once corrected for special relativity effects, is not sufficient to produce the observed UFO velocity distribution.

Particularly, we signal the possibility of a magnetocentrifugal acceleration mechanism, which is capable to drive the wind up to very high terminal velocities. Typical values are $\sim 1 - 3$ times the rotational velocity at the wind launching radius R_0 (Fukumura et al. 2010, 2014; Tombesi et al. 2013; Cui & Yuan 2020). For $R_0 = 50 r_G$, this corresponds to terminal velocities between 0.14 and 0.42 c , thus easily accounting for the observed UFO velocities.

We outline two interesting implications of our results. Several observations show the simultaneous presence in AGN X-ray spectra of fast absorbers with comparable $v_{out} \sim 0.1 - 0.2 c$ and orders of magnitude differences between their ξ (Longinotti et al. 2015; Serafinelli et al. 2019; Reeves et al. 2020). This evidence can be easily explained within our model. The weak dependence of the outflow solutions from n_0 indicates that different wind el-

ements can be launched with similar velocity (and column density) but rather different ionisation parameters, as shown in Fig. 8. This, in turn, is due to the sub-dominant contribution of the force multipliers (and then of the line driving) with respect to Thompson scattering, as outlined also in Dannen et al. (2019).

Secondly, failed winds (FW) are a natural outcome in any radiative driven scenario, and we expect their presence to be ubiquitous, if the radiation is the main driver. In fact, in our analysis we show that successful winds can be launched only through very high launching velocities ($v_{z,0} \propto v_{rot}$) or extreme luminosities $\lambda_{Edd} (\gtrsim 1)$. However, many AGNs hosting UFOs have $\lambda_{Edd} \sim 0.1$ (see Fig. 9), and such high $v_{z,0}$ are very difficult to justify in the framework of a steady-state accretion disc, unless postulating a "kick velocity" through hydrodynamic instabilities (see e.g. Janiuk & Czerny 2011 and references therein), disc magnetic reconnection (Di Matteo 1998; Ergun et al. 2020; Ripperda et al. 2020) or, again, resorting to a large scale MHD-driven outflow (see Yuan et al. 2015 for numerical simulations). Within the dynamics of the accretion-ejection system, we expect the FW to act as a shield for the gas launched at higher R_0 , possibly regulating its ionisation status and observational properties (Giustini & Proga 2019, 2020). However, we note that the effectiveness of FW in favouring the launching of more distant layers of gas has not been proven yet (Higginbottom et al. 2014; see discussion in Zappacosta et al. 2020 and references therein). FW are confined into a narrow equatorial region (i.e., their z height is \ll than the radial coordinate r , see Fig. 4), since the gravitational attraction prevents them from reaching high altitudes before bouncing back to the accretion disc, making them particularly difficult to observe. A careful modelisation of the wind duty cycle and of the disc region is needed in order to further shed light on this topic.

Finally, we note that our results are robust also in case of X-ray luminosity variability, as observed in several sources (see

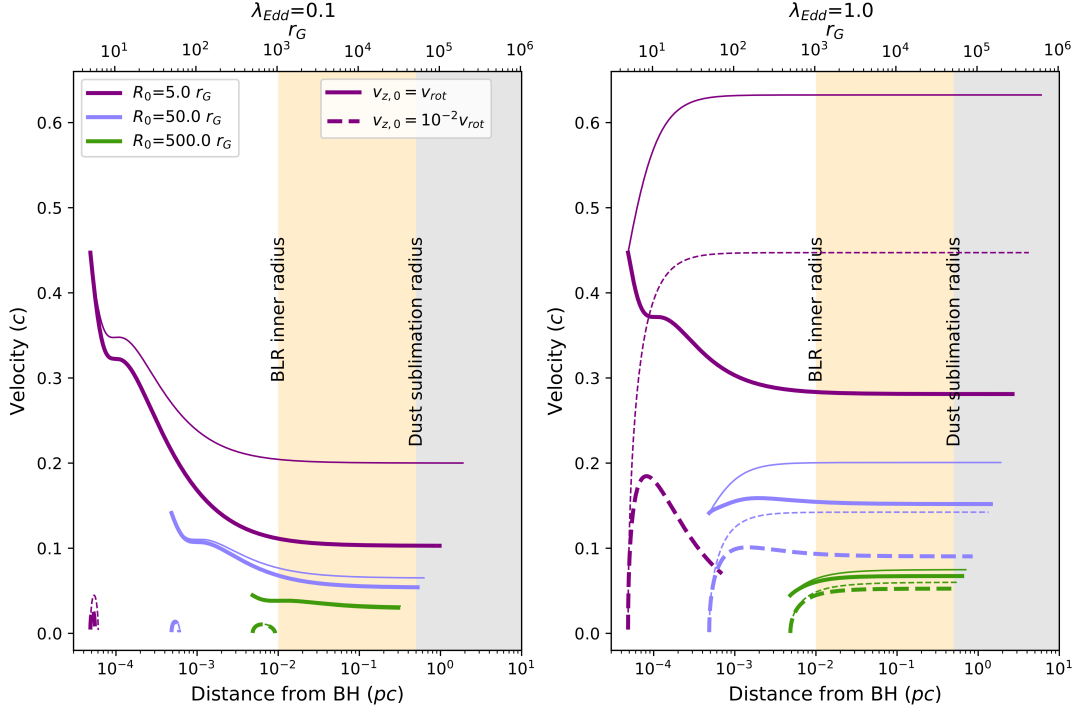


Fig. 6: Velocity vs. distance from the black hole for $\lambda_{Edd} = 0.1, 1.0$ (left and right panel, respectively). Line styles as in Fig. 4. Distances are converted from r_G to pc assuming $M = 10^8 M_{sun}$.

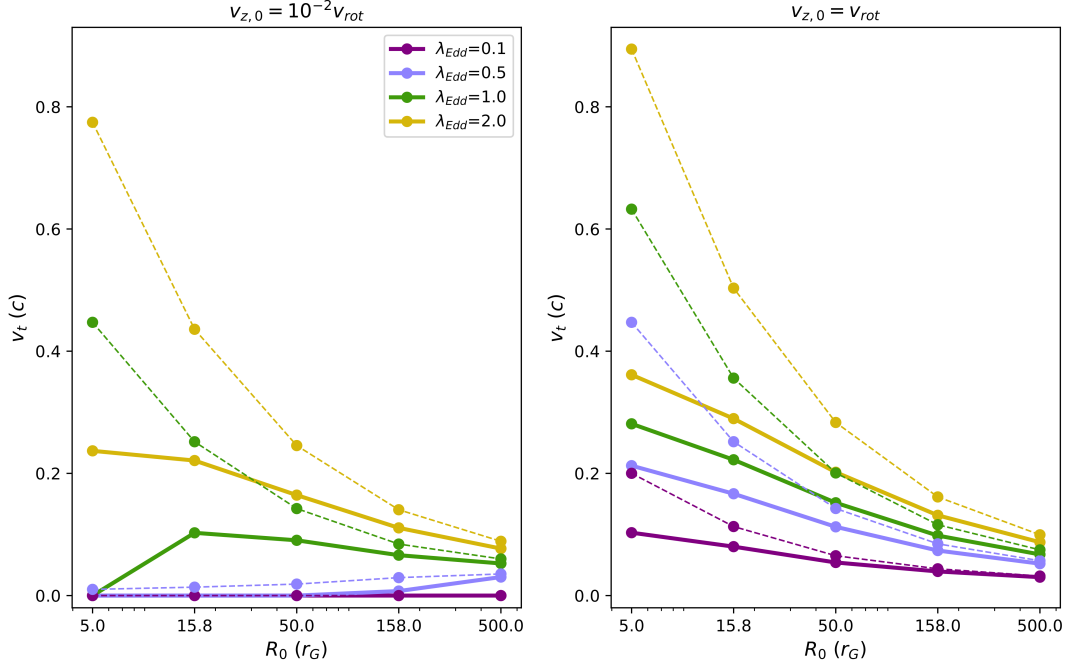


Fig. 7: Terminal velocities v_t as functions of R_0 for different values of λ_{Edd} (colour coding). Solid lines refer to the relativistic treatment, dashed to the classic (non-relativistic) one. In the left panel $v_{z,0} = 10^{-2} v_{rot}$, in the right panel $v_{z,0} = v_{rot}$.

e.g. Nardini et al. 2015; Parker et al. 2017). As discussed above, for the typical UFO ionisation degrees most of the radiative pressure is channelled through Thompson scattering, rather than line pressure. Thus, the driving luminosity is L_{bol} (expressed here as λ_{Edd}), that significantly varies in AGNs only on timescales larger

than tens of years, rather than the X-ray luminosity (expressed through λ_{UX}).

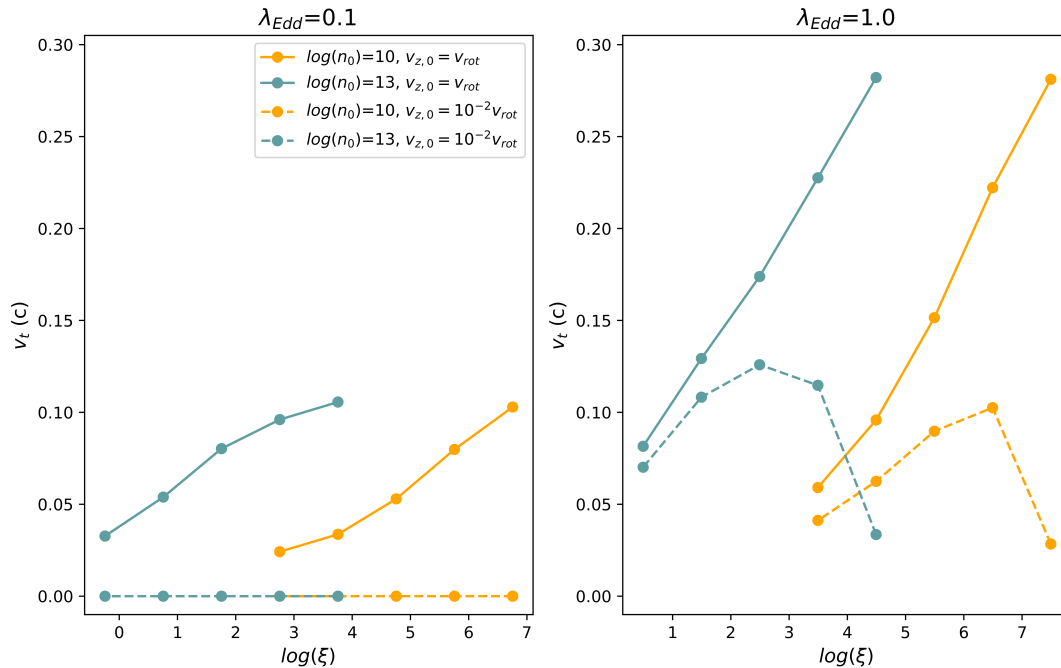


Fig. 8: v_t as functions of ξ_0 for $\log(n_0) = 10, 13$ (in units of cm^{-3} , yellow and gray lines, respectively). Solid and dashed lines refer to $v_{z,0} = v_{rot}$ and $= 10^{-2}v_{rot}$, respectively. In the left panel $\lambda_{Edd} = 0.1$, in the right panel $= 1.0$.

8. Conclusion

Special relativity effects strongly reduce the radiative pressure exerted on fast moving clumps of gas, as in the case of UFOs from accretion discs, as well as BAL winds, as discussed in the Introduction. In our work, we carried out an extensive analysis of the radiative driving for a disc wind accounting for these effects. Our main findings can be summarised as follows:

- The dynamics of the wind is primarily governed by the AGN luminosity and the launching velocity $v_{z,0}$. For high luminosity, $\lambda_{Edd} = 1.0$, the wind is successfully launched independently from $v_{z,0}$, while for $\lambda_{Edd} = 0.1$ a higher $v_{z,0}$, of the order of the disc rotational velocity, is required in order to overcome the gravitational attraction from the central black hole (see Fig. 4).
- Shortly after the launch of the wind (between one day and one month, depending on R_0), the wind attains a roughly constant velocity v_t , which is conserved until the end of the integration time ($10^6 t_G$, i.e. $10yr$ for a black hole mass of $10^8 M_{sun}$). After ~ 1 month, the wind reaches BLR-like distances, possibly suggesting an interaction with the gas in the BLR orbiting above the accretion disc.
- The inclusion of special relativity effects reduces the radiative pressure exerted on the wind. This, in turn, leads to remarkably lower v_t with respect to the classical treatment, up to 50 % less for winds launched at the smallest R_0 . Within the relativistic treatment, we find an upper limit of $v_t = 0.15c$ for the highest luminosity case ($\lambda_{Edd} = 1.0$) and a launching radius $\geq 50r_G$, in agreement with the observed UFO locations.
- Interestingly, we find that most of the UFO velocities from the literature cannot be reproduced within our radiative driving scenario. For the majority of the sources, which have λ_{Edd} between 0.03 and 1, the luminosity is too low to reproduce the observed v_{out} . This evidence suggests that other acceleration mechanisms are at play. In particular, we sug-

gest the possibility of magnetic driving, which could easily account for the observed v_{out} .

Acknowledgements. We thank the referee for the valuable comments that helped improve the paper and Manuela Bischetti for discussions on the UFO host galaxies. AL deeply thanks all the staff at the Harvard & Smithsonian Center for Astrophysics for their warm welcome during the time spent there. AL, EP, FT, LZ acknowledge financial support under ASI-INAF contract 2017-14-H.O. EP, FF acknowledge support from PRIN MIUR project "Black Hole winds and the Baryon Life Cycle of Galaxies: the stone-guest at the galaxy evolution supper", contract #2017PH3WAT

References

- Adhikari, T. P., Róžańska, A., Czerny, B., et al. 2016, *ApJ*, 831, 68
Bentz, M. C. & Manne-Nicholas, E. 2018, *ApJ*, 864, 146. doi:10.3847/1538-4357/aad808
Bischetti, M., Piconcelli, E., Feruglio, C., et al. 2019, *A&A*, 628, A118
Blandford, R. D., & Payne, D. G. 1982, *MNRAS*, 199, 883
Braito, V., Reeves, J. N., Matzeu, G. A., et al. 2018, *MNRAS*, 479, 3592
Bruni, G., Piconcelli, E., Misawa, T., et al. 2019, *A&A*, 630, A111
Caballero-García, M. D., Papadakis, I. E., Dovciak, M., et al. 2020, arXiv e-prints, arXiv:2007.00597
Caglar, T., Burtscher, L., Brandl, B., et al. 2020, *A&A*, 634, A114. doi:10.1051/0004-6361/201936321
Chartas, G., Kochanek, C. S., Dai, X., et al. 2012, *ApJ*, 757, 137
Chartas, G., Saez, C., Brandt, W. N., et al. 2009, *ApJ*, 706, 644
Chatterjee, R., Marscher, A. P., Jorstad, S. G., et al. 2011, *ApJ*, 734, 43. doi:10.1088/0004-637X/734/1/43
Coffey, D., Longinotti, A. L., Rodríguez-Ardila, A., et al. 2014, *MNRAS*, 443, 1788
Czerny, B. 2019, *Open Astronomy*, 28, 200
Contopoulos, J., & Lovelace, R. V. E. 1994, *ApJ*, 429, 139
Cui, C., & Yuan, F. 2020, *ApJ*, 890, 81
Dannen, R. C., Proga, D., Kallman, T. R., et al. 2019, *ApJ*, 882, 99
Di Matteo, T. 1998, *MNRAS*, 299, L15
Di Matteo, T., Springel, V., & Hernquist, L. 2005, *Nature*, 433, 604
Dyda, S., & Proga, D. 2018, *MNRAS*, 481, 5263

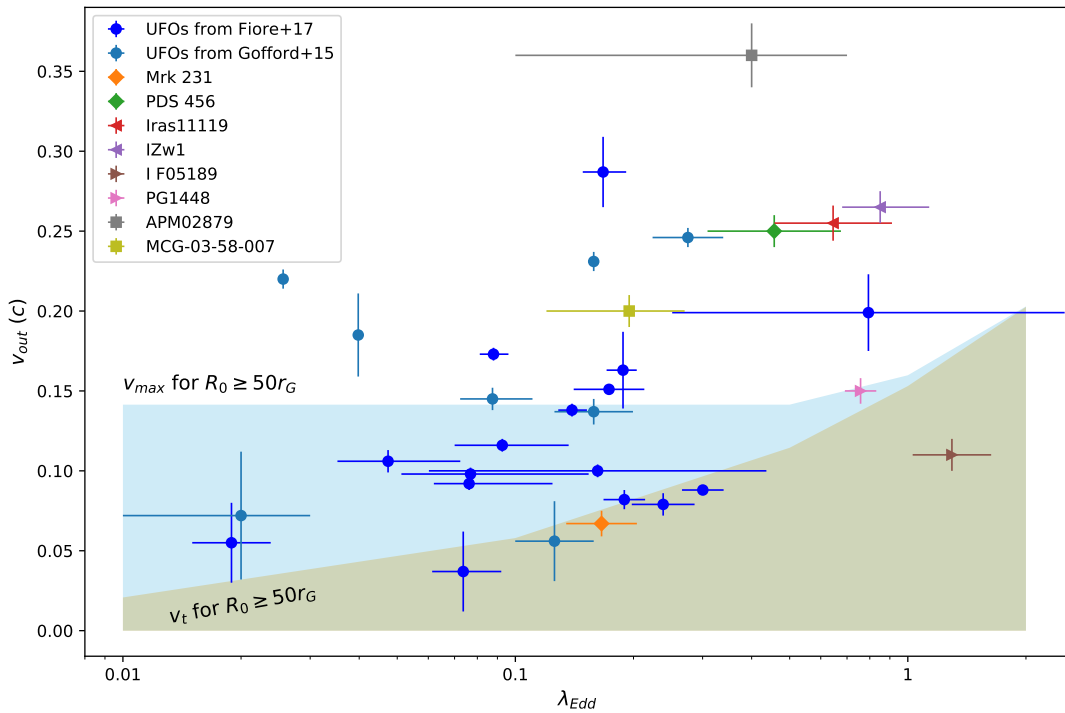


Fig. 9: Comparison between UFO velocities from the literature (dots and squares) and the results of the present work as a function of λ_{Edd} . Theoretical limit according to the terminal velocity v_t for $R_0 \geq 50r_G$ corresponds to the orange shaded area. Limit according to the maximum (but short-lived) velocity v_{max} corresponds to the light blue area. See Sect. E in Appendix for a description of the sample and the related references.

Elvis, M. 2000, *ApJ*, 545, 63
Ergun, R. E., Ahmadi, N., Kromyda, L., et al. 2020, *ApJ*, 898, 154
Ferland, G. J., Chatzikos, M., Guzmán, F., et al. 2017, *Rev. Mexicana Astron. Astrofis.*, 53, 385
Feruglio, C., Fiore, F., Carniani, S., et al. 2015, *A&A*, 583, A99
Fiore, F., Feruglio, C., Shankar, F., et al. 2017, *A&A*, 601, A143
Fukumura, K., Kazanas, D., Contopoulos, I., et al. 2010, *ApJ*, 715, 636
Fukumura, K., Tombesi, F., Kazanas, D., et al. 2014, *ApJ*, 780, 120
Fukumura, K., & Tombesi, F. 2019, *ApJ*, 885, L38
Gaspari, M., Melioli, C., Brighenti, F., et al. 2011, *MNRAS*, 411, 349
Gofford, J., Reeves, J. N., McLaughlin, D. E., et al. 2015, *MNRAS*, 451, 4169
Giustini, M. & Proga, D. 2019, *A&A*, 630, A94
Giustini, M. & Proga, D. 2020, arXiv:2002.07564
Hagino, K., Odaka, H., Done, C., et al. 2015, *MNRAS*, 446, 663
Hamann, F., Chartas, G., Reeves, J., et al. 2018, *MNRAS*, 476, 943
Higginbottom, N., Proga, D., Knigge, C., et al. 2014, *ApJ*, 789, 19
Hopkins, P. F. & Elvis, M. 2010, *MNRAS*, 401, 7
Janiuk, A. & Czerny, B. 2011, *MNRAS*, 414, 2186
Kallman, T. & Bautista, M. 2001, *ApJ Suppl.*, 133, 221
Kara, E., Alston, W. N., Fabian, A. C., et al. 2016, *MNRAS*, 462, 511
Kelly, B. C. & Bechtold, J. 2007, *ApJS*, 168, 1. doi:10.1086/509725
King, A., & Pounds, K. 2015, *ARA&A*, 53, 115
Kormendy, J., & Ho, L. C. 2013, *ARA&A*, 51, 511
Laha, S., Guainazzi, M., Dewangan, G. C., et al. 2014, *MNRAS*, 441, 2613
Laurenti, M., Luminari, A., Tombesi, F., et al. 2020, *A&A* in press, arXiv:2011.08212
Longinotti, A. L., Krongold, Y., Guainazzi, M., et al. 2015, *ApJ*, 813, L39
Luminari, A., Tombesi, F., Piconcelli, E., et al. 2020, *A&A*, 633, A55
Lusso, E., Comastri, A., Simmons, B. D., et al. 2012, *MNRAS*, 425, 623
Matthews, J. H., Knigge, C., Higginbottom, N., et al. 2020, *MNRAS*, 492, 5540
Nardini, E., Reeves, J. N., Gofford, J., et al. 2015, *Science*, 347, 860.
Nardini, E., & Zubovas, K. 2018, *MNRAS*, 478, 2274
Netzer, H. 2013, *The Physics and Evolution of Active Galactic Nuclei*, by Hagai Netzer, Cambridge, UK: Cambridge University Press, 2013
Nomura, M., Ohsuga, K., Takahashi, H. R., et al. 2016, *PASJ*, 68, 16. doi:10.1093/pasj/psv124
Nomura, M., Ohsuga, K., & Done, C. 2020, *MNRAS*, 494, 3616. doi:10.1093/mnras/staa948
Onori, F., Ricci, F., La Franca, F., et al. 2017, *MNRAS*, 468, L97. doi:10.1093/mnras/slx032
Parker, M. L., Pinto, C., Fabian, A. C., et al. 2017, *Nature*, 543, 83
Peterson, B. M., Ferrarese, L., Gilbert, K. M., et al. 2004, *ApJ*, 613, 682. doi:10.1086/423269
Piconcelli, E., Jimenez-Bailón, E., Guainazzi, M., et al. 2005, *A&A*, 432, 15
Proga, D., Stone, J. M., & Kallman, T. R. 2000, *ApJ*, 543, 686
Proga, D., & Kallman, T. R. 2004, *ApJ*, 616, 688
Quera-Bofarull, A., Done, C., Lacey, C., et al. 2020, *MNRAS*, 495, 402
Reeves, J. N., & Braitto, V. 2019, *ApJ*, 884, 80
Reeves, J. N., Braitto, V., Chartas, G., et al. 2020, *ApJ*, 895, 37
Reis, R. C., & Miller, J. M. 2013, *ApJ*, 769, L7
Reis, R. C., Reynolds, M. T., Miller, J. M., et al. 2014, *Nature*, 507, 207
Ricci, F., La Franca, F., Marconi, A., et al. 2017, *MNRAS*, 471, L41. doi:10.1093/mnras/slx103
Ricci, F., La Franca, F., Onori, F., et al. 2017, *A&A*, 598, A51. doi:10.1051/0004-6361/201629380
Ripperda, B., Bacchini, F., & Philippov, A. 2020, arXiv:2003.04330
Risaliti, G., & Elvis, M. 2010, *A&A*, 516, A89
Różańska, A., Nikolajuk, M., Czerny, B., et al. 2014, *New Astronomy*, 28, 70
Rybicki, G. B., & Lightman, A. P. 1986, *Radiative Processes in Astrophysics*, Chapter 1
Saez, C., & Chartas, G. 2011, *ApJ*, 737, 91
Saturni, F. G., Bischetti, M., Piconcelli, E., et al. 2018, *A&A*, 617, A118
Schurch, N. J. & Done, C. 2007, *MNRAS*, 381, 1413. doi:10.1111/j.1365-2966.2007.12336.x
Shakura, N. I., & Sunyaev, R. A. 1973, *A&A*, 500, 33
Serafinelli, R., Tombesi, F., Vagnetti, F., et al. 2019, *A&A*, 627, A121
Sim, S. A., Proga, D., Miller, L., et al. 2010, *MNRAS*, 408, 1396
Smith, R. N., Tombesi, F., Veilleux, S., et al. 2019, *ApJ*, 887, 69
Sturm, E., Dexter, J., Pfuhl, O. et al. 2018, *Nature* 563, 657–660
Szanecki, M., Niedzwiecki, A., Done, C., et al. 2020, arXiv e-prints, arXiv:2006.15016
Tilton, E. M. & Shull, J. M. 2013, *ApJ*, 774, 67. doi:10.1088/0004-637X/774/1/67
Tombesi, F., Cappi, M., Reeves, J. N., et al. 2011, *ApJ*, 742, 44
Tombesi, F., Cappi, M., Reeves, J. N., et al. 2012, *MNRAS*, 422, L1
Tombesi, F., Cappi, M., Reeves, J. N., et al. 2013, *MNRAS*, 430, 1102
Tombesi, F., Meléndez, M., Veilleux, S., et al. 2015, *Nature*, 519, 436
Vestergaard, M. & Peterson, B. M. 2006, *ApJ*, 641, 689. doi:10.1086/500572
Yuan, F., Gan, Z., Narayan, R., et al. 2015, *ApJ*, 804, 101
Zappacosta, L., Piconcelli, E., Giustini, M., et al. 2020, *A&A*, 635, L5

Appendix A: Three-dimensional wind

We show in Fig. A.1 a detailed analysis of the wind trajectories for the preliminary three-dimensional model presented in Sect. 3.

Appendix B: Geometrical and physical properties of the wind

We show in Fig. B.1 (first three panels) the geometrical thickness of the wind. With our density profile $n(r) = n_0 \left(\frac{r_0}{r}\right)^2$ (see Sect. 5), the upper limit for the column density corresponds to $N_{H,max} = n_0 r_0$. For all the values of n_0, r_0 in this paper, $N_{H,max} > 10^{24} \text{ cm}^{-2}$. The only exception is for $n_0 = 10^{10} \text{ cm}^{-3}, r_0 = 5r_G$ (first panel, blue line), for which $N_{H,max} = 7.4 \cdot 10^{23} \text{ cm}^{-2}$. In the last panel of Fig. B.1 we plot $\xi(r)$ for $\lambda_{Edd} = 0.1, 1.0$.

Fig. B.2 shows f_{rad} as a function of N_H , for different R_0 (colour coding) and $\log(n_0/\text{cm}^3) = 10, 11, 12, 13$ (from left to right). From top to bottom, $\lambda_{Edd} = 0.1, 0.5, 1.0, 2.0$.

Appendix C: Dependence of the wind dynamics on n_0, N_H

To give an idea of the impact of n_0 on the wind dynamics, we show in Fig. C.1 the terminal velocity v_t as a function of R_0 for different n_0 (colour coding). From left to right, $\lambda_{Edd} = 0.1, 0.5, 1.0, 2.0$. Top (bottom) row refers to $v_{z,0} = v_{rot} (v_{z,0} = 10^{-2} v_{rot})$. v_t is similar for any value of n_0 , except for $v_{z,0} = 0.01 v_{rot}$ and $\lambda_{Edd} = 0.5, 1.0$, where the initial velocity is low enough (and the luminosity is not too low nor too high) so that different f_{rad} values can give rise to different wind behaviours.

Similarly, in Fig. C.2 we plot v_t for $\log(n_0/\text{cm}^3) = 10, 13$ for the lower and upper values of N_H ($5 \cdot 10^{22}$ and 10^{24} cm^{-2}). It can be seen that the overall dynamics of the wind is weakly sensitive to N_H .

Appendix D: Results

We present in Fig. D.1 a detailed analysis of the wind dynamics for $\lambda_{Edd} = 1, v_{z,0} = v_{rot}, \log(n_0/\text{cm}^3) = 11, N_H = 10^{23} \text{ cm}^{-2}$ and taking into account the wind opacity (Sect. 4).

Appendix E: Notes on UFOs sources from literature

We show in Table E.1 the properties of the sources plotted in Fig. 9. The sample is composed of three main groups. The first one is taken from the Tombesi et al. (2011) sample, with the updated L_{bol} from Fiore et al. (2017), while the second one is from Gofford et al. (2015). The third one comprises the sources reported in Fiore et al. (2017) and not previously reported in Tombesi et al. (2011), together with other individually-reported UFOs published from 2017 on for which robust estimates of both λ_{Edd} and v_{out} are available. Where possible, the black hole mass M and the AGN bolometric luminosity L_{bol} have been updated with recent works, listed in the last column.

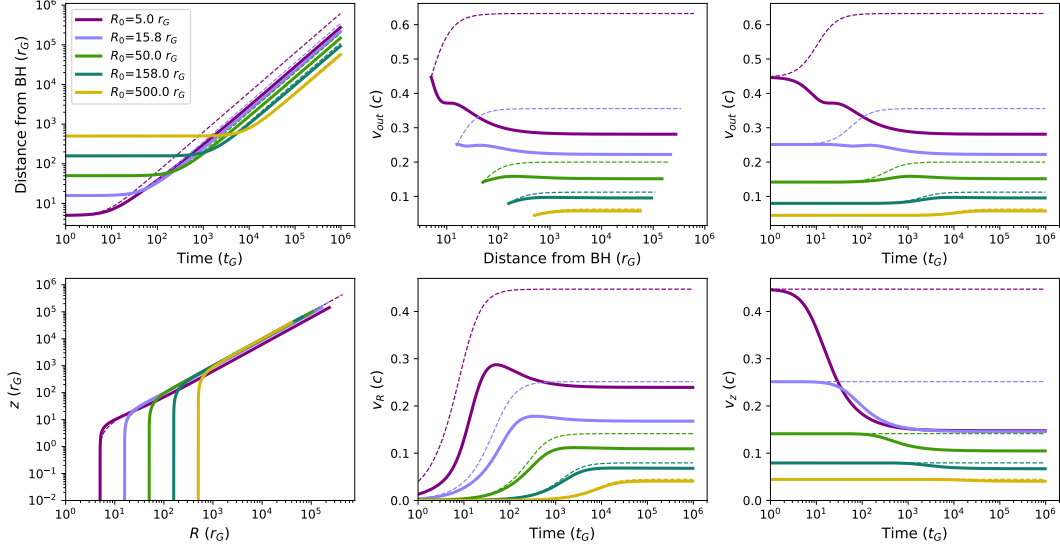


Fig. A.1: Wind trajectories for $v_{z,0} = v_{rot}$ and $\lambda_{Edd} = 1$. From top to bottom and left to right: distance r from the BH (where $r = \sqrt{R^2 + z^2}$) as a function of t ; outflow velocity v_{out} as a function of r ($v_{out} = \sqrt{v_R^2 + v_z^2}$); v_{out} as a function of t ; trajectories of the wind in the $z - R$ plane; v_R (radial velocity) as a function of t ; v_z (vertical velocity) as a function of t . Solid(dashed) lines refer to the relativistic(classic) treatment.

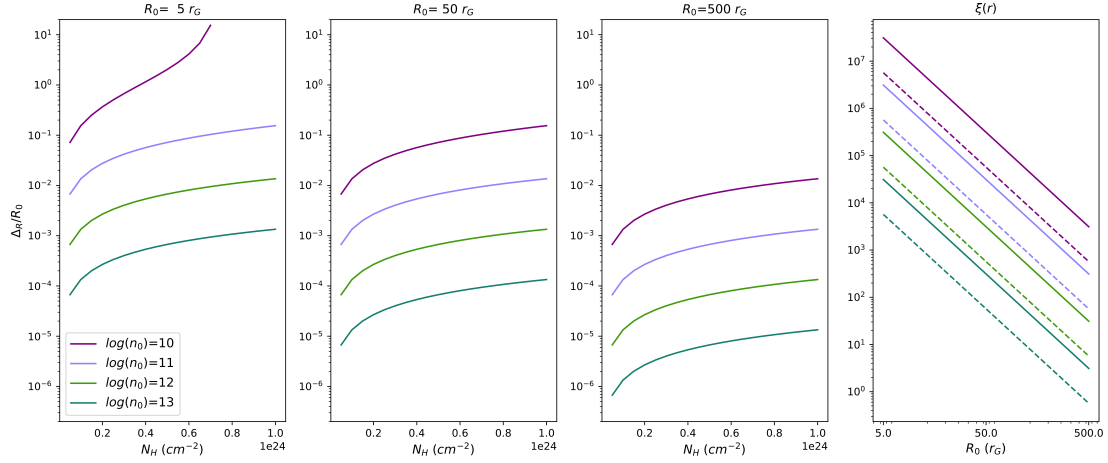


Fig. B.1: First three panels: geometrical thickness of the wind as a function of N_H for $\log(n_0) = 10, 11, 12, 13$ (in units of cm^{-3} , colour coding) and increasing R_0 (from left to right). Last panel: ionisation parameter as a function of R_0 for different $\log(n_0)$ (colour coding) and $\lambda_{Edd} = 0.1, 1.0$ (dashed and solid lines, respectively).

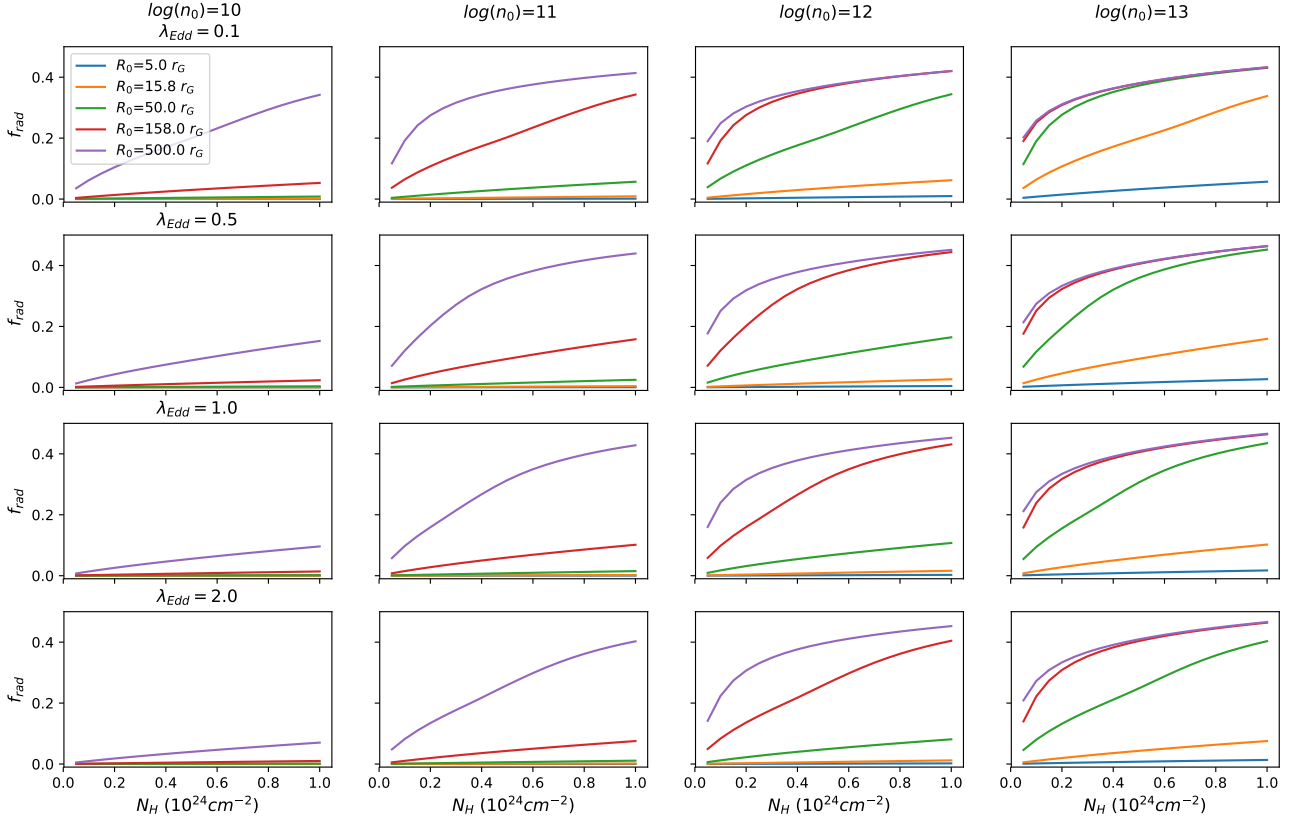


Fig. B.2: Values of f_{rad} as functions of N_H for $\log(n_0) = 10, 11, 12, 13$ (in units of cm^{-3} , from left to right) and $\lambda_{Edd} = 0.1, 0.5, 1.0, 2.0$ (from top to bottom).

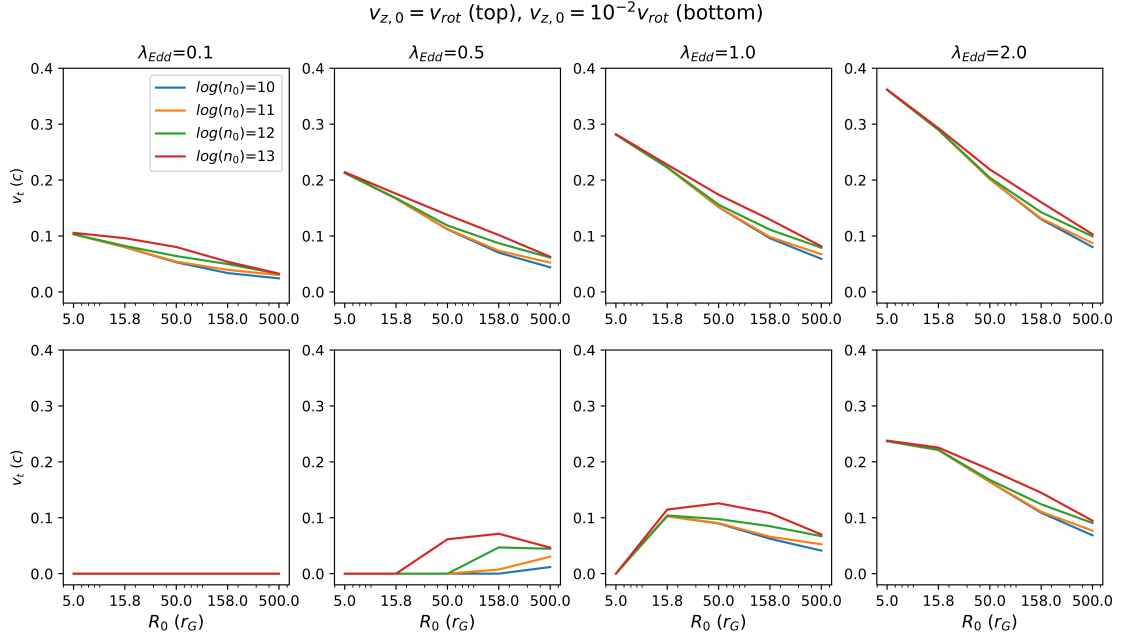


Fig. C.1: Terminal velocity of the wind for $\log(n_0) = 10, 11, 12, 13$ (in units of cm^{-3} , colour coding) and for different luminosities (from left to right $\lambda_{Edd} = 0.1, 0.5, 1.0, 2.0$). In the top(bottom) panel $v_{z,0} = v_{rot}$ ($v_{z,0} = 10^{-2}v_{rot}$). For simplicity, we fix $N_H = 10^{23}cm^{-2}$.

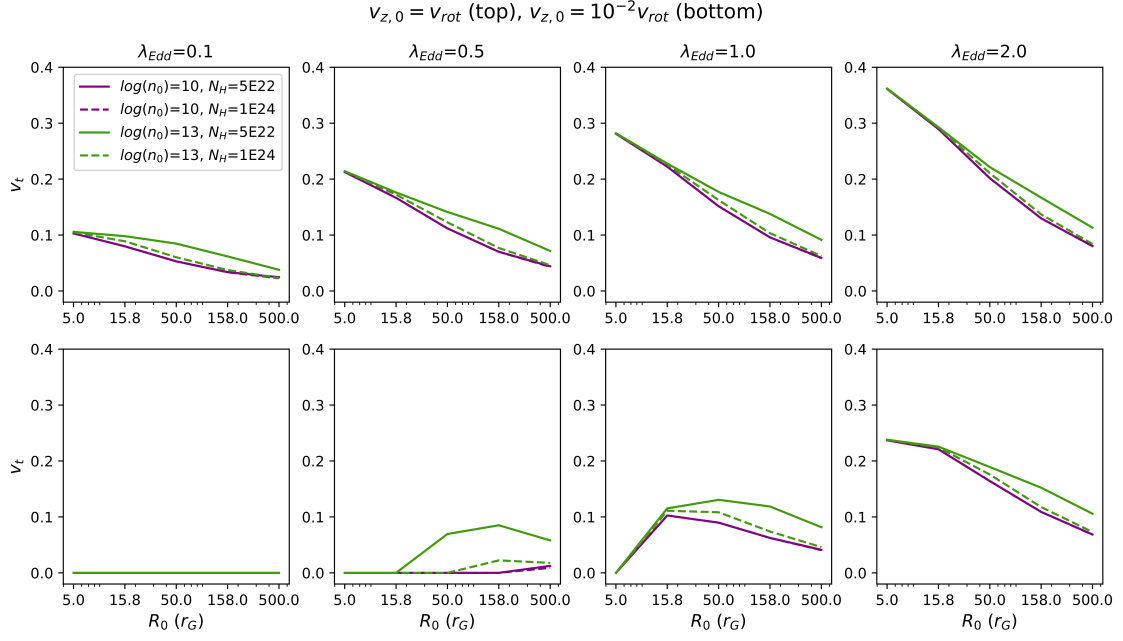


Fig. C.2: Terminal velocity of the wind for $\log(n_0) = 10, 13$ (in units of cm^{-3} , purple and green lines) and $N_H = 5 \cdot 10^{22}$ and $= 10^{24}$ (in units of cm^{-2} , solid and dashed lines). In the top(bottom) panel $v_{z,0} = v_{rot}$ ($v_{z,0} = 10^{-2}v_{rot}$).

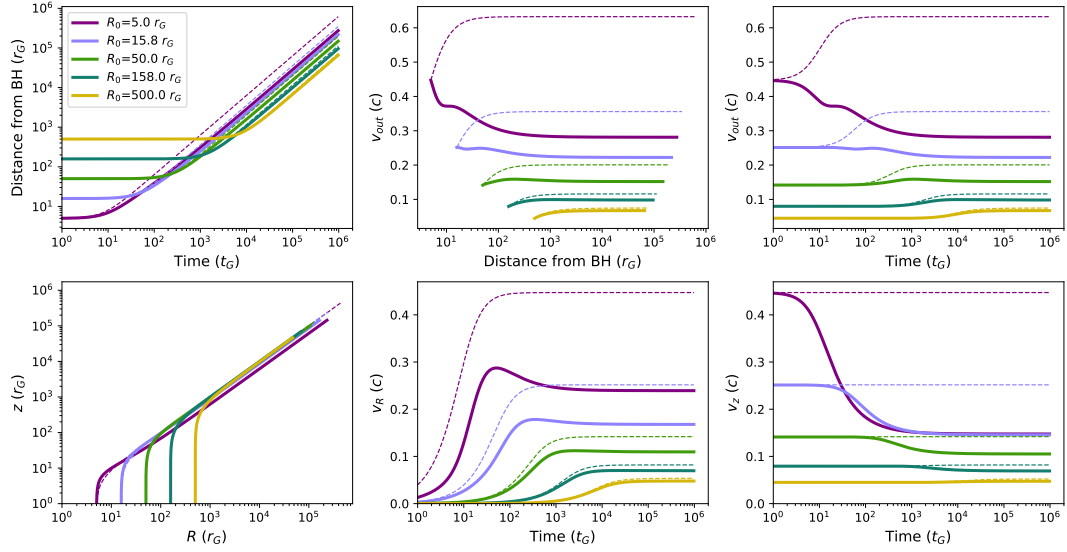


Fig. D.1: Wind solutions in the relativistic and classic cases (solid and dashed lines, respectively) for $\lambda_{Edd} = 1$, $v_{z,0} = v_{rot}$ and taking into account the wind opacity. Meaning of the panels as in Fig. A.1

Group	Name	λ_{Edd}	v (c)	Refs.
1	NGC4151	0.05 ± 0.01	0.106 ± 0.007	A
	IC4329A	0.08 ± 0.03	0.098 ± 0.004	
	Mrk509	0.09 ± 0.01	0.173 ± 0.004	A
	Mrk509	0.14 ± 0.01	0.138 ± 0.004	A
	ARK120	0.17 ± 0.02	0.29 ± 0.02	A
	Mrk79	0.08 ± 0.01	0.092 ± 0.004	B
	NGC4051	0.07 ± 0.01	0.04 ± 0.02	B
	Mrk766	0.19 ± 0.02	0.082 ± 0.006	C
	Mrk766	0.30 ± 0.03	0.088 ± 0.002	C
	Mrk841	0.02 ± 0.00	0.06 ± 0.02	D
	1H0419-577	0.24 ± 0.04	0.079 ± 0.007	E
	Mrk290	0.19 ± 0.02	0.16 ± 0.02	B
	Mrk205	0.16 ± 0.10	0.100 ± 0.004	F
	PG1211+143	0.17 ± 0.03	0.151 ± 0.003	D
	MCG-5-23-16	0.09 ± 0.02	0.116 ± 0.004	G
	NGC4507	0.79 ± 0.54	0.20 ± 0.02	
2	3C111	0.02 ± 0.01	0.07 ± 0.04	H
	3C3903	0.09 ± 0.02	0.145 ± 0.007	A
	4C+74.26	0.04 ± 0.00	0.18 ± 0.03	
	ESO103-G035	0.13 ± 0.03	0.06 ± 0.03	
	MR2251-178	0.16 ± 0.03	0.137 ± 0.008	
	Mrk279	0.03 ± 0.00	0.220 ± 0.006	B
	NGC5506	0.28 ± 0.05	0.246 ± 0.006	I
	SQJ2127	0.16 ± 0.00	0.231 ± 0.006	
3	Mrk231	0.17 ± 0.03	0.067 ± 0.008	L,M
	PDS456	0.46 ± 0.15	0.25 ± 0.01	N
	Iras 11119	0.65 ± 0.19	0.26 ± 0.01	L,O
	IZwicky1	0.85 ± 0.17	0.27 ± 0.01	P
	Iras 05189	1.30 ± 0.27	0.110 ± 0.010	Q,R
	PG1448	0.76 ± 0.077	0.150 ± 0.008	S
	APM08279	0.40 ± 0.30	0.36 ± 0.02	T,U
	MCG-03-58-007	0.20 ± 0.07	0.20 ± 0.01	V

Table E.1: Sources plotted in Fig. 9. From left to right, columns indicate the number of the group, the source name, λ_{Edd} , the UFO velocity v_{out} (in units of c) and the additional references for each source. Group 1: UFO v_{out} and black hole mass M from Tombesi et al. (2012), L_{bol} from Fiore et al. (2017). Group 2: values from Gofford et al. (2015). For both groups, M , L_{bol} have been updated (where possible) with recent values from the literature, see reference column. Group 3: individual sources, see reference column. References: A Peterson et al. (2004), B Ricci et al. (2017), C Bentz & Manne-Nicholas (2018), D Vestergaard & Peterson (2006), E Tilton & Shull (2013), F Kelly & Bechtold (2007), G Caglar et al. (2020), H Chatterjee et al. (2011), I Ricci et al. (2017), L Nardini & Zubovas (2018), M Feruglio et al. (2015), N Nardini et al. (2015), O Tombesi et al. (2015), P Reeves & Braitto (2019), Q Smith et al. (2019), R Onori et al. (2017), S Laurenti et al. (2020), T Chartas et al. (2009), U Saturni et al. (2018), V Braitto et al. (2018)